Supporting information for: "Resonant Silicon Nanoparticles for Enhancement of Light Absorption and Photoluminescence from Hybrid Perovskite Films and Metasurfaces"

E. Tiguntseva, A. Chebykin, E.V. Ushakova, F. Komissarenko, V. Milichko, A. Tsypkin, D. Zuev, and S. Makarov
ITMO University, St. Petersburg 197101, Russia

A. Ishteev
National University of Science and Technology MISiS, Moscow, 119049, Russia and aITMO University, St Petersburg 197101, Russia.

R. Haroldson, B. Balachandran, H. Wang, and W. Hu
University of Texas at Dallas, Richardson, Texas 75080, United States

A. Zakhidov
ITMO University, St. Petersburg 197101, Russia and
University of Texas at Dallas, Richardson, Texas 75080, United States

CONTENTS

Mie scattering from nanoparticles in air and perovskite 2
Electric field enhancement near the c-Si and TiO$_2$ nanoparticles in perovskite 4
Time-resolved analysis of photoluminescence kinetics 8
Atomic force microscopy characterization of perovskite surface and metasurface 9
References 9

Mie scattering from nanoparticles in air and perovskite

We performed a series of analytical calculations in the Matlab software, following the theory of Mie scattering [1]. In the Mie theory, absorption C_{abs} cross-section for spherical nanoparticles (NPs) is linked with extinction and scattering cross-sections $C_{abs} = C_{ext} - C_{sca}$, where C_{ext} and C_{sca} are following:

$$C_{sca} = \frac{W_{sca}}{I} = \frac{2\pi}{k^2}\sum_{n=1}^{\infty}(2n+1)(|a_n|^2 + |b_n|^2), \tag{1}$$

$$C_{ext} = \frac{W_{ext}}{I} = \frac{2\pi}{k^2}\sum_{n=1}^{\infty}(2n+1)Re(a_n + b_n), \tag{2}$$

where W_{sca}, W_{ext} are the scattered and extinct powers by nanosphere, respectively, $k = 2\pi n_r/\lambda$, n_r is the refractive index, I is the incident intensity, a_n and b_n are the scattering coefficients that describe interaction of the nanoparticle with a plane wave. Magnetic permeabilities of the surrounding media and nanoparticles are equal to one in the optical range. These assumptions lead to simplified form of the scattering coefficients:

$$a_n = \frac{m\psi_n(mx)\psi'_n(x) - \psi_n(x)\psi'_n(mx)}{m\psi_n(mx)\xi'_n(x) - \xi_n(x)\psi'_n(mx)}, \tag{3}$$

$$b_n = \frac{\psi_n(mx)\psi'_n(x) - m\psi_n(x)\psi'_n(mx)}{\psi_n(mx)\xi'_n(x) - m\xi_n(x)\psi'_n(mx)}, \tag{4}$$

with $x = ka$, and the Riccati - Bessel functions : $\psi_n(\rho) = \rho j_n(\rho)$, $\xi_n(\rho) = \rho h_n^{(1)}(\rho)$, where j_n and $h_n^{(1)}$ are spherical Bessel and Hankel functions, respectively.

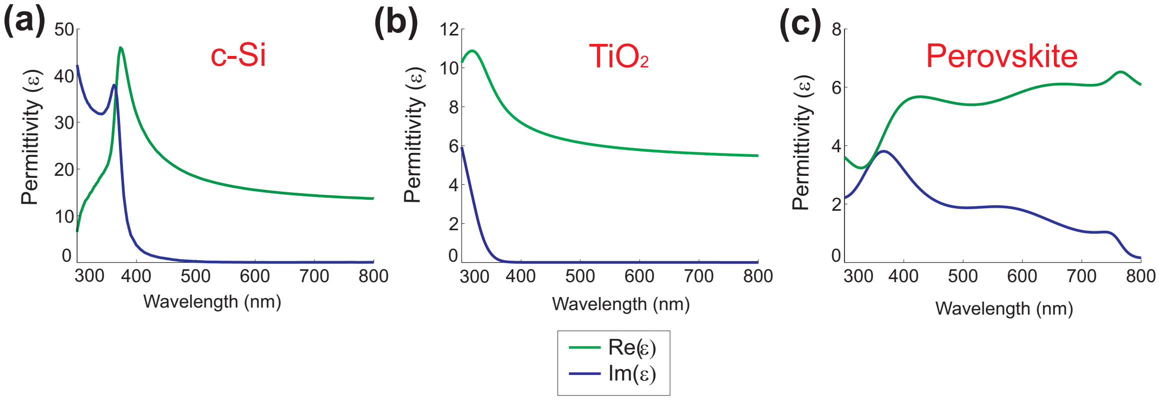

FIG. S1. Real (green curves) and imaginary (blue curves) parts of dielectric permittivity for (a) crystalline silicon (c-Si), (b) titanium dioxide (TiO$_2$) and (c) perovskite (MAPbI$_3$).

In order to describe optical properties of nanoparticles from different basic materials for perovskite-based photovoltaics and optoelectronics, we use tabular values of dielectric permittivity for crystalline silicon (c-Si) [2], titanium

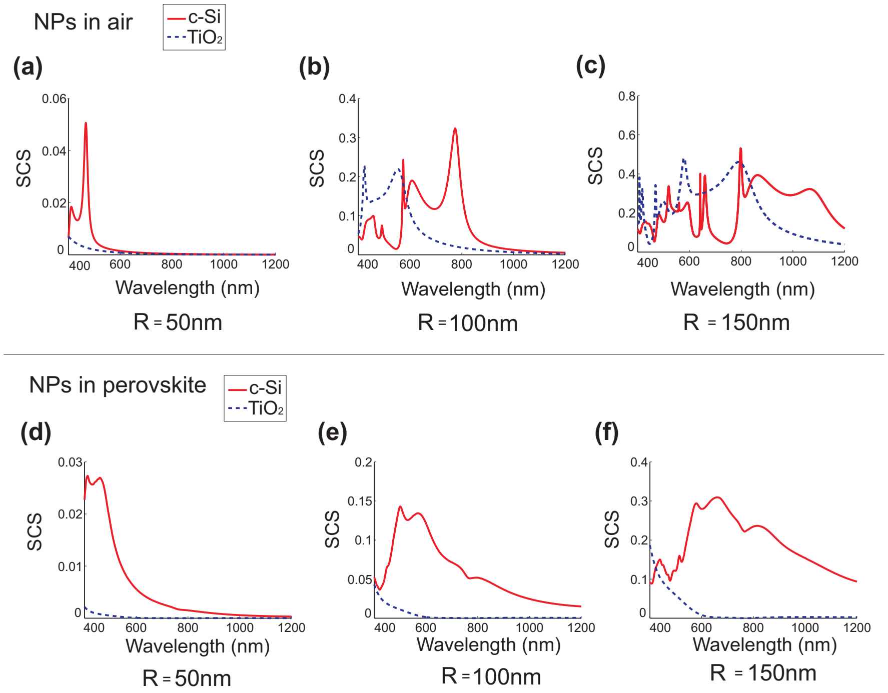

FIG. S2. A comparison of the c-Si and TiO_2 NPs scattering cross-sections (SCS) spectra for three different particle radii (R): (a-c) particle in air, (d-e) particle in perovskite.

oxide (TiO_2) [2], and halide perovskite $CH_3NH_3PbI_3$ (or $MAPbI_3$) [3], which are shown in Fig. S1. TiO_2 nanoparticles are used for comparison with c-Si ones, because of their widespread application in organic and perovskite based solar cells [4, 5].

In the Fig.S2 scattering cross section (SCS) spectra of single -Si and TiO_2 NPs in air and in perovskite for the radii of nanoparticles of 50, 100, and 150 nm are shown. As can be seen from the figure, the resonance frequency shifts to the long-wave region with increasing of particle radius. In Fig.S2c, when the particle is surrounded by air the SCS of the -Si and TiO_2 NPS are comparable in the region of 800 nm wavelengths. However, in the case when the nanoparticle is located in the perovskite (Fig.S2d-e), the SCS of the TiO_2 nanoparticle has values close to 0 in the entire IR range. At the same time, for the c-Si nanoparticle, the SCS values in the near-IR range are about 0.25.

For a more detailed analysis of the NPs SCS spectra in air and perovskite, we carry out decomposition of the modes (Fig.S3 and Fig.S4). As can be seen from the figures Fig.S3c,f,i,l, if the nanoparticle is located in air, significant contribution to the scattering at $\lambda \approx 800$ nm for $R = 150$ nm is given both by the magnetic and electric dipole Mie-type resonances for the cases of c-Si or TiO_2 NPs. However, in Fig.S4(g-l) it can be seen that when TiO_2 nanoparticle is placed in the perovskite, no excitation of electric or magnetic dipole resonances is observed in the near-IR range, which leads to practically zero scattering in this range for all values of the radius R. This effect is related to small optical contrast between TiO_2 and $MAPbI_3$, according to Fig. S1b,c. At the same time, the picture for c-Si nanoparticles (Fig.S4a-f) is different: although the resonances strongly broadened, we still observe rather strong scattering in the near-IR range for the radii 100 and 150 nm.

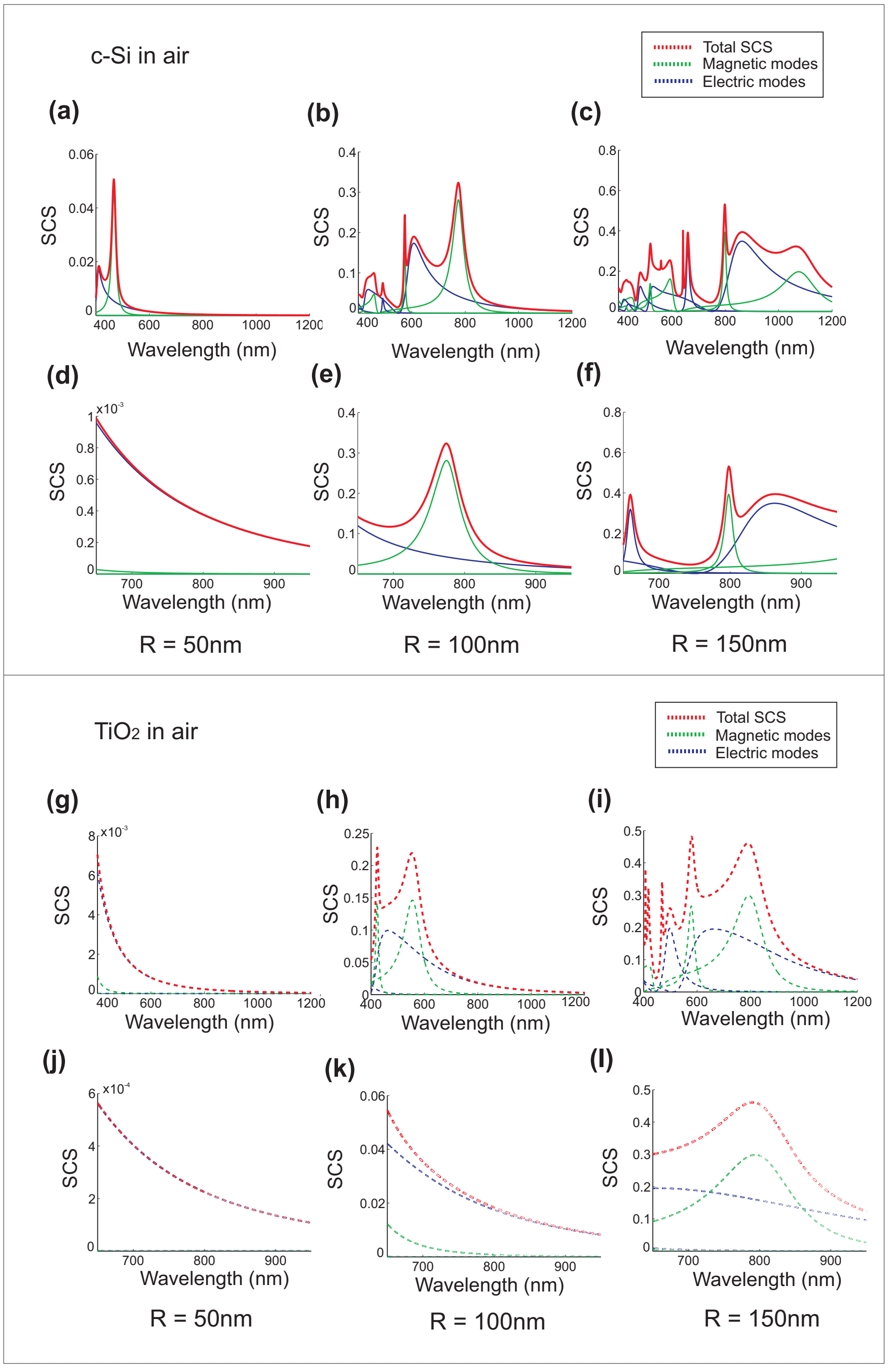

FIG. S3. Mode decomposition for Si (a-f) and TiO_2(g-l) NPs in air for three different particle radii (R). Figures (d–f) and (j–l) illustrate more narrow spectral range (λ=650–950 nm).

Electric field enhancement near the c-Si and TiO_2 nanoparticles in perovskite

We have calculated numerically in the CST Microwave Studio the dependencies of the field enhancement on the diameter of a single nanoparticle placed inside and on the surface of the infinity perovskite. The probes of the E field were placed at a distance of 5 nm from the spherical nanoparticle in the perovskite, as shown in Fig.S5b,c. A plane wave linearly polarized in the plane of the picture fell on the particle along the normal. As it can be seen from the Fig.S5a, the contrast in the refractive indices between c-Si and perovskite is higher compared to the contrast between the perovskite and TiO_2, the field intensifies are stronger in the case of c-Si nanoparticles practically in the whole

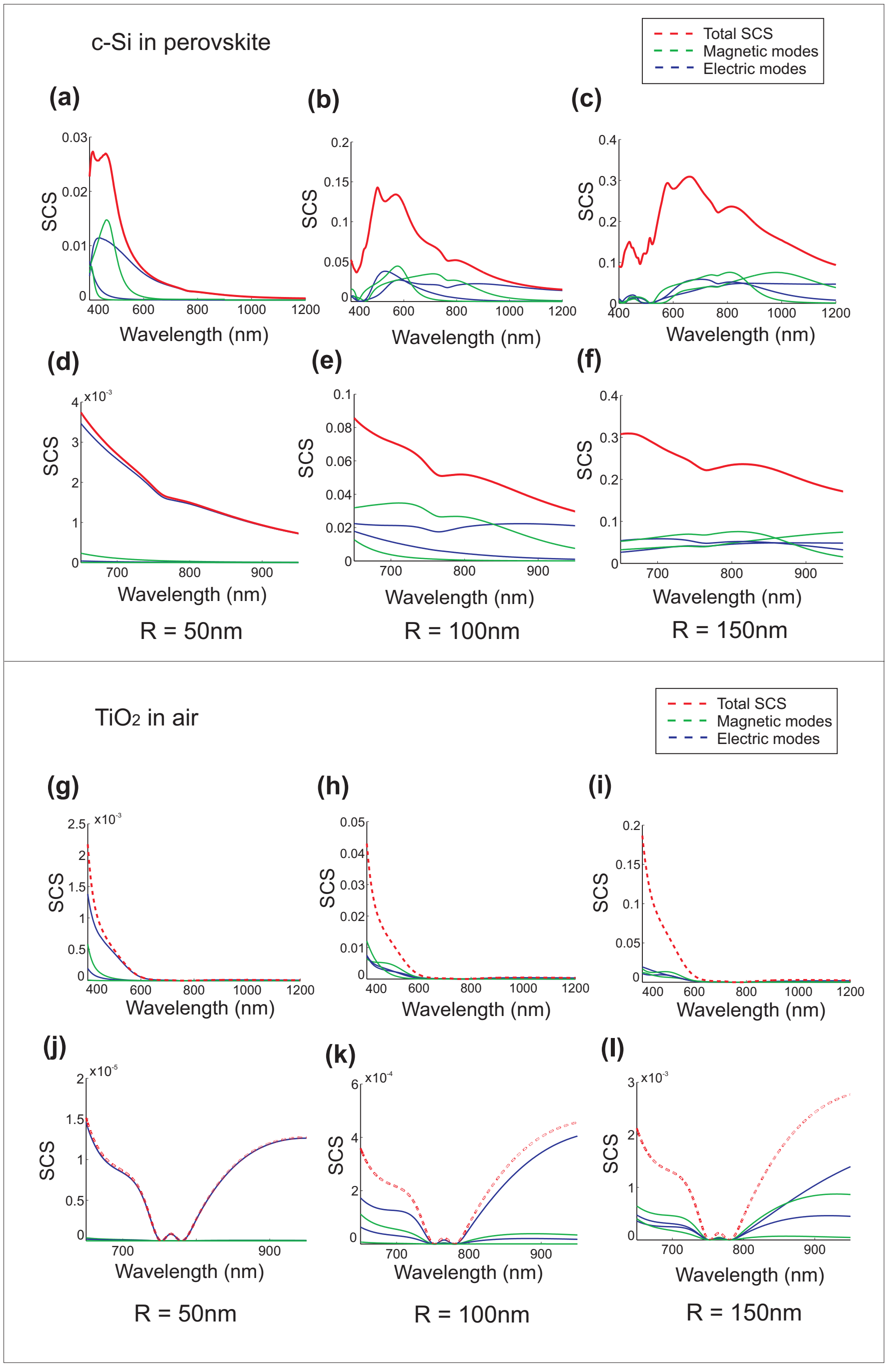

FIG. S4. Mode decomposition for Si (a-f) and TiO_2(g-l) nanoparticles in perovskite for three different particle radii (R). Figures (d–f) and (j–l) illustrate more narrow spectral range (λ=650–950 nm).

range of diameters for both cases. The red curves on Fig.S5a correspond to the c-Si nanoparticle, the blue curves correspond to the TiO_2 nanoparticle, while the solid curves correspond to the nanoparticles inside the perovskite, the dashed curves correspond to the nanoparticles on the surface of the perovskite. The Fig.S5d-g show the E field distributions for TiO_2 (d,h) and c-Si (e,g) nanoparticles with a radius of 145 nm at a wavelength of 775 nm inside the perovskite and at the perovskite surface in air. Moreover, the electric field near the TiO_2 nanoparticle can even be smaller than incident one, as shown Fig.S5a,d. At D = 290 nm, the E field is stronger for the c-Si nanoparticle compared to the TiO_2 nanoparticle up to 4 times (when they are embedded in the perovskite), and up to 1.8 times for the nanoparticles on the perovskite surface.

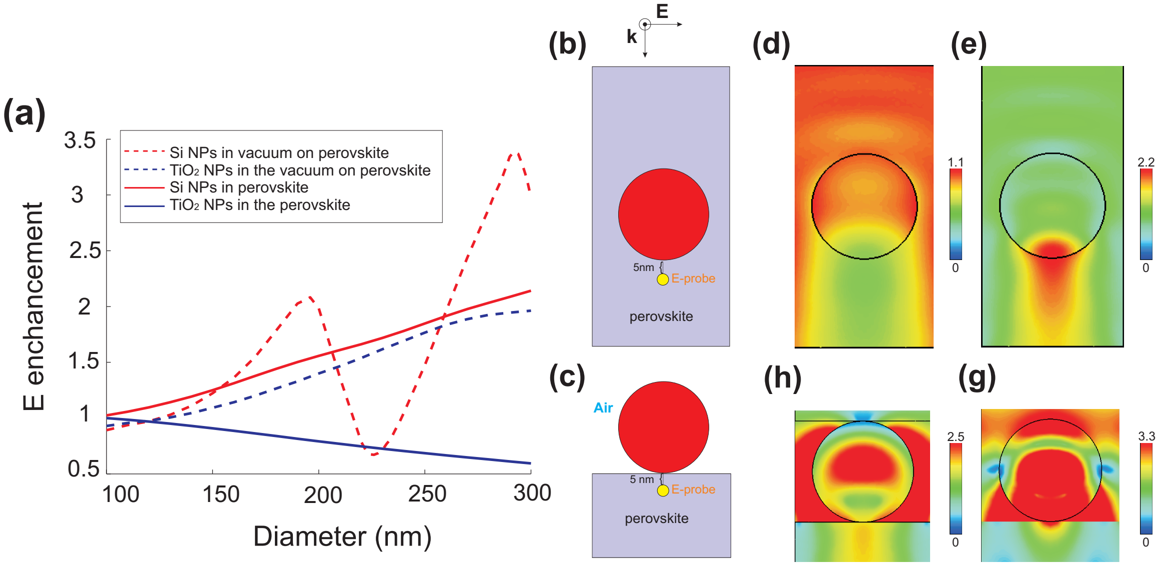

FIG. S5. The dependence of the electric field enhancement (in amplitude) near the c-Si and TiO_2 NPs on diameter of the nanoparticle (a). Field calculation schemes for the case of particles inside the perovskite (b) and on the perovskite surface (c). Electric field distributions for TiO_2 (d, h) and c-Si (e, g) NPs with a radius of $R = 145$ nm at a wavelength of 775 nm for the cases of NPs inside and on the surface. Color bars indicate local electric fields normalized to the incident one from a plane wave in the perovskite $|E|/|E_0|$.

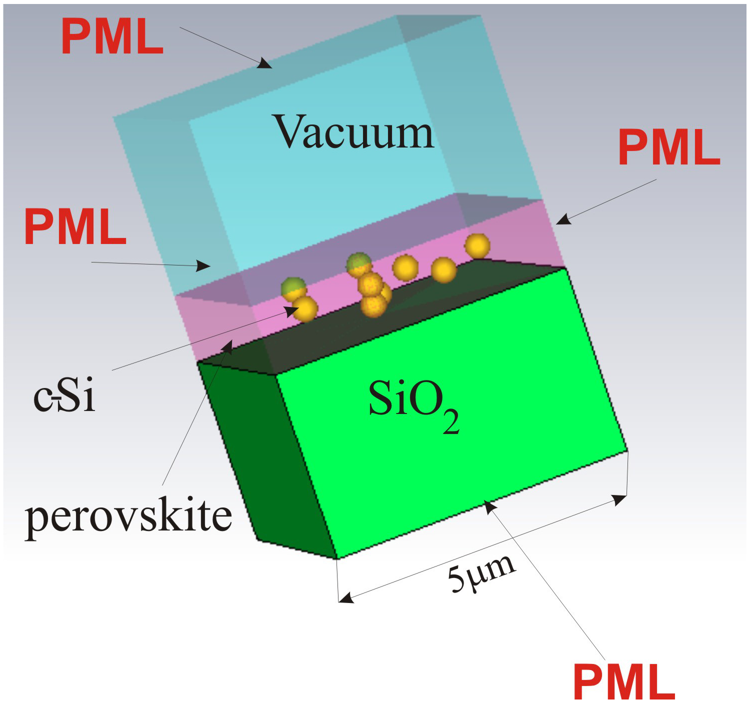

FIG. S6. Illustration of boundary conditions which are used for simulations of absorbance spectra in Lumerical FDTD Solutions.

In order to answer the question about distinguishing of absorption in perovskite from that in Si nanoparticles, we carry out additional simulations of the absorption spectra in Lumerical FDTD Solutions. Computation volume is illustrated in Fig. S6, where Si nanoparticles are distributed over the volume of the perovskite film with a thickness of 800 nm, and their concentration corresponds to experimental one. When simulating the absorption spectra, we use the PML (Perfect Matched Layered) boundary conditions, as shown in Fig.S6. The dimensions of the sample in the transverse directions were $5{\times}5\mu$m. When the radius of the nanoparticles is changing, their number also changing in order to the ratio of the volumes occupied by the nanoparticles to the volume of the perovskite film remained constant.

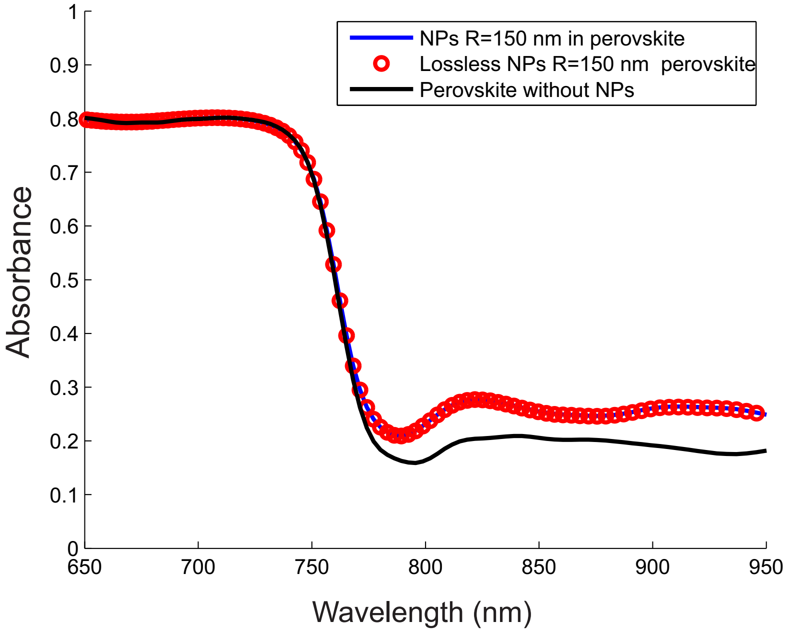

FIG. S7. Numerically calculated absorbance spectra for a 800 nm $MAIPb_3$ perovskite film (black line), the same film with c-Si NPs inside the perovskite (blue line) and with lossless c-Si NPs inside perovskite (red circles).

Fig.S7 shows a comparison of absorption spectra for the perovskite film without nanoparticles (black curve), for perovskite with embedded silicon nanoparticles with real losses (blue curve) and for perovskite with silicon nanoparticles with zero imaginary part of the permittivity (red circles). The calculation is carried out for nanoparticles with radius R = 150 nm. As it is clearly seen from the figure, losses in c-Si nanoparticles practically do not affect the absorption spectrum, which indicates that light absorption takes place in the perovskite material mostly.

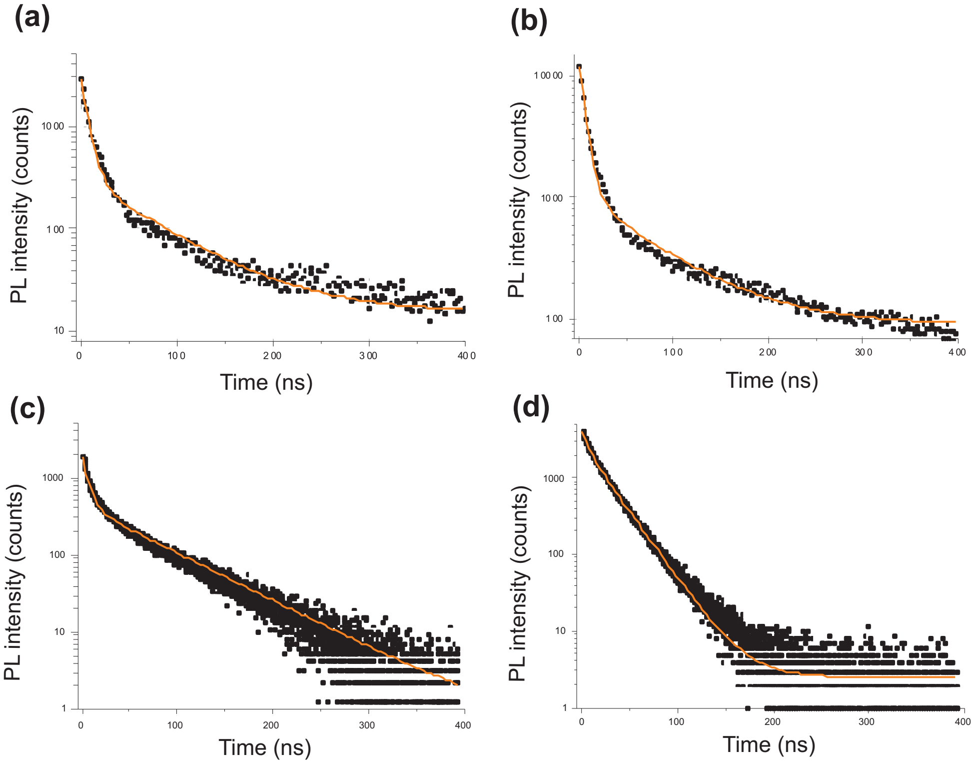

FIG. S8. Photoluminescence decays and their biexponential approximations for different location of the c-Si NPs to the perovskite film: (a,c) bare films, (b) film with -Si nanoparticles on top of the film, (d) film with -Si nanoparticles inside.

Time-resolved analysis of photoluminescence kinetics

Generally, the kinetics of carriers recombination in perovskite is described by the following formula [6]:

$$\frac{dn}{dt} = -k_r n - k_t n - \gamma n^3 \tag{5}$$

where n is the photogenerated carrier density and t is time. We can ascribe each term in equation (5) to physical charge carrier annihilation processes following photoexcitation of the $\mathrm{MAPbI_3}$ thin film: (i) the radiative recombination rate, (ii) a monomolecular decay $\mathrm{k}_t n$ to describe carrier trapping, and (iii) the electronhole annihilation rate via non-radiative Auger processes, proportional to γn^3. In our experiments with $\mathrm{MAPbI_3}$, we use biexponential law, because the Auger recombination is negligible upon weak laser intensity I = 2.85 W/cm^2 [6]:

$$n(t) = a_1 exp(-t/t_1) + a_2 exp(-t/t_2) \tag{6}$$

Average PL lifetime is calculated with:

$$t_{average} = \frac{\sum_i \mathrm{a_i} t_i^2}{\sum_i \mathrm{a_i} t_i}, \tag{7}$$

where a_i is the partial amplitude of PL with the decay time t_i. In order to eliminate instrument response function (IRF) of our measuring system, we take a fixed delay of 3 ns. Table 1 represents fitting parameters for photoluminescence decay for all our samples. In series 2 we observe dynamic PL quenching: the incorporating of Si NPs inside perovskite film caused the formation of additional channels of nonradiative charge carrier recombination.

TABLE I.

Sample name	a_1	t_1	a_2	t_2	$t_{average}$
	weighted	ns	weighted	ns	ns
1 series					
bare perovskite film	0,89	$7,2 \pm 0,5$	0,11	70 ± 2	$40,7 \pm 2,0$
Si NPs at bare perovskite film	0,91	$6,5 \pm 0.5$	0,09	70 ± 2	$38,7 \pm 2,0$
2 series					
bare perovskite film	0,79	$6,0 \pm 0,5$	0,21	70 ± 2	$54,5 \pm 2,0$
Si NPs inside perovskite film	0,33	$6,3 \pm 0,5$	0,67	$24,6 \pm 1,0$	$22,5 \pm 1,0$

Atomic force microscopy characterization of perovskite surface and metasurface

For AFM characterization we use an atomic force microscope stage (SmartSPM AIST-NT) and a micrometer stage (3-axis flexure stage Thorlabs MBT616D). According to our measurements, the perovskite metasurface depth varies from 260 to 300 nm, period varies from 610 to 630 nm. Roughness of an initial perovskite film is nearly 50-60 nm.

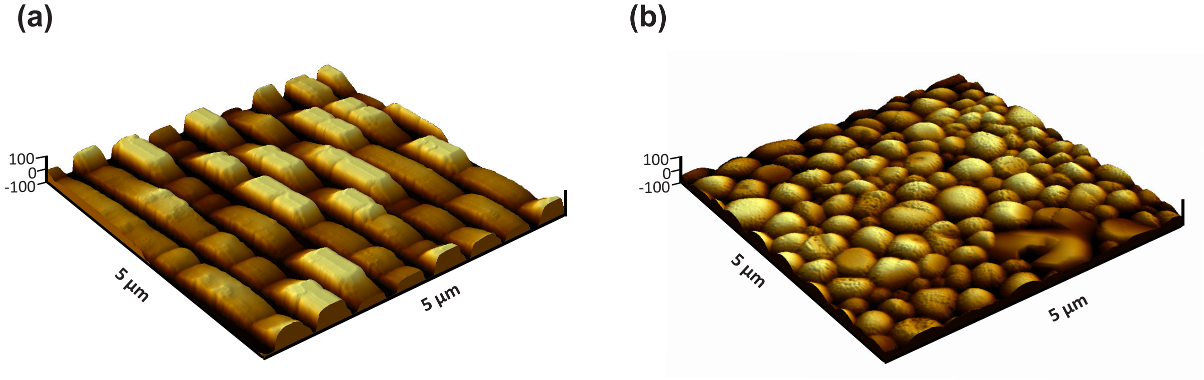

FIG. S9. AFM image of perovskite metasurface (a) and perovskite initial film (b).

---

[1] C. F. Bohren and D. R. Huffman, *Absorption and scattering of light by small particles* (John Wiley & Sons, 2008).
[2] E. D. Palik, *Handbook of optical constants of solids*, Vol. 3 (Academic press, 1998).
[3] L. J. Phillips, A. M. Rashed, R. E. Treharne, J. Kay, P. Yates, I. Z. Mitrovic, A. Weerakkody, S. Hall, and K. Durose, Data in brief **5**, 926 (2015).
[4] L. Etgar, P. Gao, Z. Xue, Q. Peng, A. K. Chandiran, B. Liu, M. K. Nazeeruddin, and M. Gratzel, Journal of the American Chemical Society **134**, 17396 (2012).
[5] J. Yin, H. Qu, J. Cao, H. Tai, J. Li, and N. Zheng, RSC Advances **6**, 24596 (2016).
[6] M. Saba, M. Cadelano, D. Marongiu, F. Chen, V. Sarritzu, N. Sestu, C. Figus, M. Aresti, R. Piras, A. G. Lehmann, *et al.*, Nature Communications **5**, 5049 (2014).